ACS OMEGA

Open Access

http://pubs.acs.org/journal/acsodf

Article

PB_{12}^{+} and $P_2B_{12}^{+/0/-}$: The Novel B_{12} Cage Doped by Nonmetallic P Atoms

Shi-Xiong Li,* Yue-Ju Yang, and De-Liang Chen

Cite This: *ACS Omega* 2023, 8, 44831−44838

Read Online

ACCESS | Metrics & More | Article Recommendations | Supporting Information

ABSTRACT: A new kind of nonmetallic atom-doped boron cluster is described herein theoretically. When a phosphorus atom is added to the B_{12} motif and loses an electron, a novel B_{12} cage is obtained, composed of two B_3 rings at both ends and one B_6 ring in the middle, forming a triangular bifrustum. Interestingly, this B_{12} cage is formed by three B_7 units joined together from three directions at an angle of 120°. When two P atoms are added to the B_{12} motif, this novel B_{12} cage is also obtained, and two P atoms are attached to the B_3 rings at both ends of the triangular bifrustum, forming a triangular bipyramid (Johnson solid). Amazingly, the global minimums of neutral, monocationic, and monoanionic $P_2B_{12}^{+/0/-}$ have the same cage structure with a D_{3h} symmetry; this is the smallest boron cage with the same structure. The P atom has five valence electrons, according to adaptive natural density partitioning bonding analyses of cage PB_{12}^{+} and P_2B_{12}, in addition to one lone pair, the other three electrons of the P atom combine with an electron of each B atom on the B_3 ring to form three 2c−2e σ bonds and form three electron sharing bonds with B atoms through covalent interactions, stabilizing the B_{12} cage. The calculated photoelectron spectra can be compared with future experimental values and provide a theoretical basis for the identification and confirmation of $P_nB_{12}^{-}$ (n = 1−2).

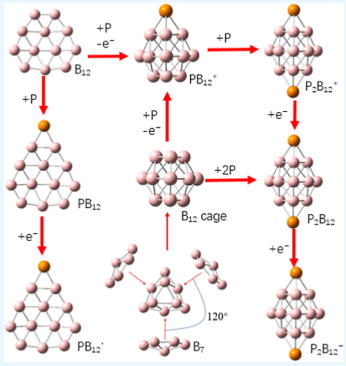

1. INTRODUCTION

The structures and characteristics of clusters, which are unique aggregates of two or more atoms joined by ionic, metallic, or covalent bonds, differ from those of bulk materials. The cluster study has gained popularity in the field of physical chemistry. The multicenter bond property is present in pure boron clusters made up of boron atom with three valence electrons and anionic B_n^{-} (n < 38) exhibit planar or quasi-planar forms,[1,2] and small (n < 16) cationic or neutral boron clusters exhibit quasi-planar or planar forms.[3] The ground-breaking discovery of borospherene[4] B_{40}^{-} in 2014 sparked a plethora of boron cluster research studies.[5−9] The fundamental unit that formed the two-dimensional borophene that was synthesized experimentally in 2015 was a B_7 cluster.[10] Interestingly, a hydrogenated B_7 cluster turned out to be the fundamental structural unit in the experimental synthesis of borophene crystal form, which was produced in 2021 and comparable to graphene.[11]

Recently, the geometrical configuration and characteristics of boron clusters doped with metal atoms have been the primary focus of research.[12−21] The insertion of metal atoms has the ability to regulate the boron cluster's geometrical configuration, which in turn modifies the cluster's chemical and physical characteristics. Although it is difficult for small or medium size (n < 20) pure boron clusters to form cage structures, the addition of metal atoms can cause dramatic structural changes in boron clusters, resulting in the formation of boron cage. For example, transition or alkali metal atoms doping can adjust the boron clusters to the cage structure ($La_3B_{18}^{-}$, Sc_3B_{20}, Li_3B_{12}, Ta_4B_{18}, and $Ta_3B_{12}^{-}$).[22−26] From these studies, we know that the electron transfer from electropositive elements can cause structural transition from one shape to another and that the interaction between dopant atoms and boron cages is almost electrostatic in nature. A recent study showed that four Be atoms can induce B_{12} to become an Archimedean sphere,[27] through the covalent interaction of the Be atom with the B atoms. However, the characteristic of these cage structures is that both the dopants and B atoms are integral parts of the cage surface. In other words, the addition of these dopants does not induce a separate boron cage structure, in which the dopants are either embedded or externally attached to the boron cage. The question now is whether nonmetallic elements can also cause, such dramatic structural changes in small or medium-sized boron clusters, and in particular whether they can induce cage-type boron clusters? However, there has not been as much research on boron clusters doped with nonmetallic atoms.[28−33] Previous studies have shown that nonmetallic elements do not induce a unique cage structure. Can nonmetallic dopants induce a separate B_{12} cage structure for a typical B_{12} motif?

Received: August 14, 2023
Revised: October 26, 2023
Accepted: November 6, 2023
Published: November 16, 2023

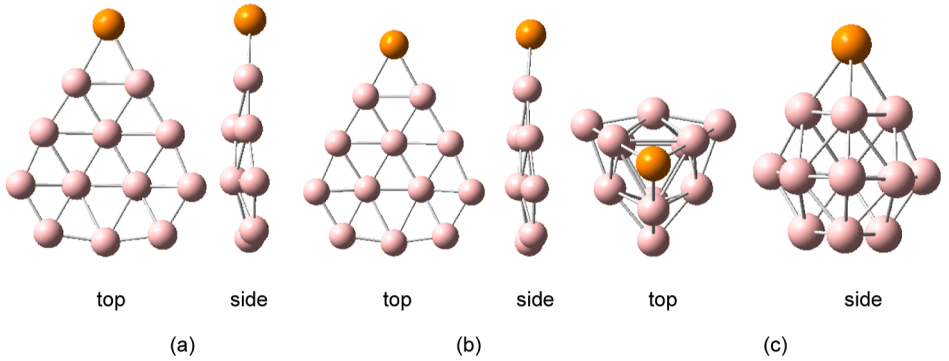

Figure 1. Structures of P atom-doped boron clusters $PB_{12}^{+/0/-}$. (a) PB_{12} C_s; (b) PB_{12}^- C_s; and (c) PB_{12}^+ C_{3v}.

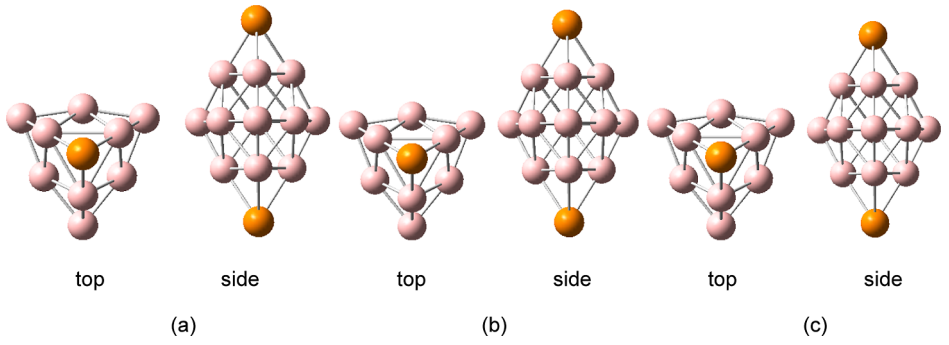

Figure 2. Structures of double P atom-doped boron clusters $P_2B_{12}^{+/0/-}$. (a) P_2B_{12} D_{3h}; (b) $P_2B_{12}^-$ D_{3h}; and (c) $P_2B_{12}^+$ D_{3h}.

Herein, the study of P-atom-doped boron clusters will fill the vacancy of doped boron clusters in this respect. We present the novel B_{12} cage doped by P atoms, in which P atoms are no longer integral parts of the cage surface, but are attached to the cage. The B_{12} framework is a perfect hollow cage in the shape of a triangular bifrustum and represents a brand new geometric structure.

2. COMPUTATIONAL DETAILS

Using the particle swarm optimization (CALYPSO) program, geometrical configuration searches of P atom-doped boron clusters $P_nB_{12}^{+/0/-}$ (n = 1−2) were carried out.[34] CALYPSO is a highly effective cluster geometrical configuration search approach that has been used to boron clusters or doped boron clusters.[35,36] For the preliminary geometric configuration search, the PBE0/3-21G level was employed. PSO procedures generated 70% of the structures in each generation, while the remaining 30% were formed randomly. When the number of phosphorus atoms is equal to 1, nearly 2000 isomers are generated for each cluster. When the number of phosphorus atom is equal to 2, nearly 3000 isomers generated for each cluster.

Low-energy structures of each cluster were then fully optimized at the PBE0/6-311+G(d) and TPSSh/def2-TZVP levels.[37−40] To obtain more accurate relative energies, CCSD(T)[41] calculations [CCSD(T)/6-311+G(d)//PBE0/6-311+G(d)] with the optimized PBE0 geometries were performed for the collected isomers. After the geometry optimizations, harmonic frequency analyses and electronic structure analyses were carried out at the PBE0/6-311+G(d) level. The PBE0/6-311+G(d) is reliable calculation level for the boron cluster,[4,19,21,42−44] specifically, computational [at the PBE0/6-311+G(d) level] photoelectron spectrum of the B_{40}^- is in excellent agreement with the experimental data.[4] So, the PBE0/6-311+G(d) level serves as the calculation method for the research in this paper. Gaussian 16 software was used for all calculations.[45] Multiwfn 3.8 code[46] in combination with VMD[47] were used to perform relevant analyses and isosurface map drawings.

3. RESULTS AND DISCUSSION

3.1. Structures and Electronic Properties. Figures S1−S6 display five low-energy structures of P atoms doped boron clusters $P_nB_{12}^{+/0/-}$ (n = 1−2), while Figure 1 and 2 display the lowest energy structures of $P_nB_{12}^{+/0/-}$ (n = 1−2). According to previous theoretical and experimental investigations, planar or quasi-planar geometrical configurations are exhibited in small (n < 16) neutral, cationic, and monoanionic boron clusters. It can be seen in Figure 1 and the calculation results that after adding one P atom, the lowest energy structures of $PB_{12}^{0/-}$ have a skeleton of pure boron clusters, $B_{12}^{0/-}$; one P atom is connected to two boron atoms of the pure boron clusters B_{12} and B_{12}^-.[3] One particular case to point out is PB_{12}^+, as shown in Figure S7, while the DFT and MP2 methods favor the cage structure, the CCSD(T) method favors the quasi-planar structure. Previous theoretical studies indicate that the quasi-planar structure for B_{40}^- is the global minimum,[4] at the DFT and CCSD methods, the quasi-planar structure has lower energy than the cage structure. However, experimental and theoretical studies reveal the existence of cage-like and quasi-planar configurations for B_{40}^-.[4] Similarly, it is possible to find the cage structure and quasi-planar structure of PB_{12}^+ experimentally. Because a large number of studies have shown that B_{12} with single-atom doping have a quasi-planar structure or half-sandwich structure, a novel cage structure is obtained in this study; this paper will highlight the cage structure, so only the cage structure PB_{12}^+ is discussed in the following analysis. Boron is electron deficient, and small (n <

https://doi.org/10.1021/acsomega.3c06002
ACS Omega 2023, 8, 44831−44838

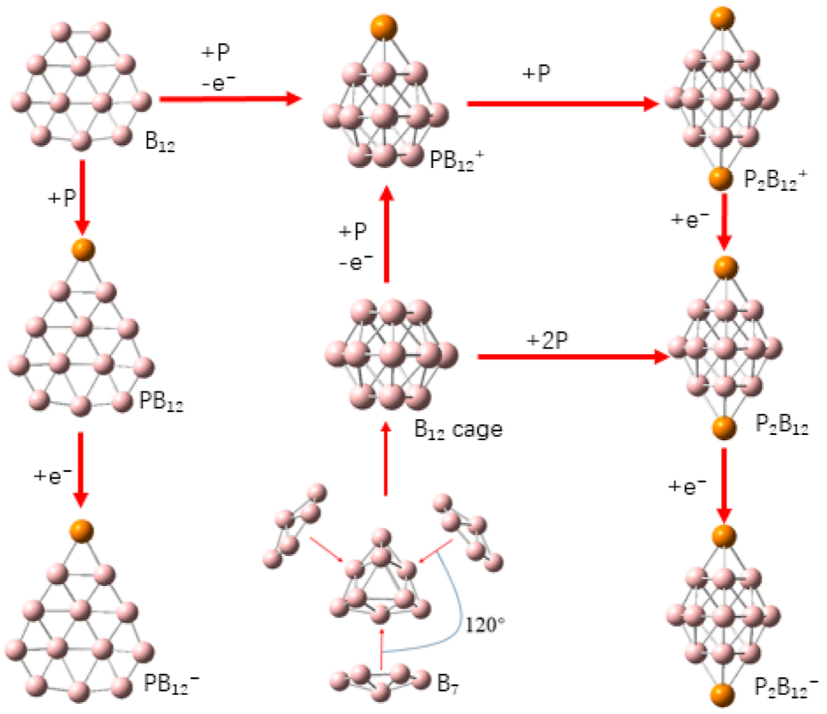

Figure 3. Regulation of boron clusters by one and two P atoms.

16) neutral, monocationic, and monoanionic pure boron clusters have difficulty in forming cages. As can be seen in Figure 3, one P atom doping can cause the cationic cluster PB_{12}^{+} to a novel cage structure with a C_{3v} symmetry, the B_{12} cage is composed of two B_3 rings at both ends and one B_6 ring in the middle, and is just a triangular bifrustum. Amazingly, as shown in Figure 3, this B_{12} cage is formed by three B_7 units joined together in three directions at an angle of 120°. Interestingly, the addition of two P atoms can adjust the quasi-planar pure boron clusters $B_{12}^{+/0/-}$ and produce triangular bipyramid (Johnson solids) clusters $P_2B_{12}^{+/0/-}$, and the lowest energy structures of neutral, monocationic, and monoanionic clusters $P_2B_{12}^{+/0/-}$ are exactly based on the structure of PB_{12}^{+}, and each P atom is attached to a B_3 ring at either end of the triangular bifrustum. $P_2B_{12}^{+/0/-}$ exhibit a high symmetry of D_{3h}. The smallest reported cage boron clusters (Li_3B_{12}, $Ta_3B_{12}^{-}$, and $Be_4B_{12}^{+}$)[25−27] exhibit a characteristic that dopants and B atoms are integral parts of the cage surface and are adjusted by multiple metal atoms. Here, a nonmetallic P atom can adjust a separate B_{12} cage, where the P atom is not an integral part of the cage surface. In addition, in the existing studies on boron clusters or doped boron clusters, there is no case of a global minimum of neutral, monocationic, and monoanionic clusters showing the same cage structure at the same time. Here, two P atom-doped B_{12} clusters $P_2B_{12}^{+/0/-}$ just fill this vacancy.

Geometrical parameters of $P_2B_{12}^{+/0/-}$ are shown in Figure S8. $P_2B_{12}^{+/0/-}$ has four different types of B−B bonds and a type of B−P bond. While the B−B bond lengths are in a range of 1.57−2.02 Å, similar to B−B bond lengths of B_7 (1.57−1.74 Å); however, the B−B bond lengths (1.95−2.02 Å) of $P_2B_{12}^{+/0/-}$ on the B_3 ring at both ends of the triangular bifrustum are much longer than the B−B bond length (1.62 Å) at the corresponding position of B_7. Furthermore, the P−B bond lengths of $P_2B_{12}^{+/0/-}$ are about 1.89−1.92 Å (see Figure S8). As can be seen in Figure 2, two P atoms are located at opposite ends of the molecule and the distance between the two P atoms is just a measure of the length of the molecule. As can be seen in Figure S8, the P−P distances of $P_2B_{12}^{+/0/-}$ are mainly in the range of 0.57−0.58 nm, and these clusters show promise for future applications in single-molecule devices because the two P atoms are at the two ends of the molecule, which can be employed as a bridge connecting gold electrodes in a molecular device.

The lowest harmonic frequency analysis confirmed that these lowest energy structures are indeed stable (no imaginary frequency). Molecular dynamics (MD) simulations were carried out with an extended Lagrangian MDs trajectory method that employs atom-centered basis functions and density matrix propagation[48,49] at 400 K. Each simulation ran for 3 ps with a step size of 0.5 fs from the equilibrium global minimum structure. As shown in Figure S9, the small root mean square deviation (RMSD) values in a range of 0.15 Å are maintained in all trajectories, suggesting that no isomerization or other structural alterations occur in a simulation of 3 ps and showing that cage structures of PB_{12}^{+} and $P_2B_{12}^{+/0/-}$ are dynamically stable.

For the closed-shell cluster, the HOMO−LUMO energy gaps of PB_{12}^{+}, PB_{12}^{-}, and P_2B_{12} are 3.63, 2.71, and 3.51 eV, respectively. For open-shell clusters, the α-HOMO−LUMO and β-HOMO−LUMO energy gaps vary within the range of 2.16−4.23 eV. Figure S10 shows the selected canonical molecular orbitals (CMOs) for $P_2B_{12}^{+/0/-}$. Figure S10a shows the HOMO and LUMO diagrams of P_2B_{12}. HOMO is contributed by phosphorus atoms and adjacent boron atoms, and LUMO is contributed by six boron atoms in the middle of the triangular bipyramid. Figure S10b shows the CMOs of $P_2B_{12}^{+}$. The α-HOMO of $P_2B_{12}^{+}$ and the HOMO of P_2B_{12} have the same isosurface diagrams because the HOMO orbital of P_2B_{12} becomes the single occupied α-HOMO of $P_2B_{12}^{+}$ after losing an electron from the HOMO orbital of P_2B_{12}. Similarly, the α-HOMO of $P_2B_{12}^{+}$, the β-LUMO of $P_2B_{12}^{+}$ and the HOMO of P_2B_{12} have the same isosurface diagrams because

https://doi.org/10.1021/acsomega.3c06002
ACS Omega 2023, 8, 44831−44838

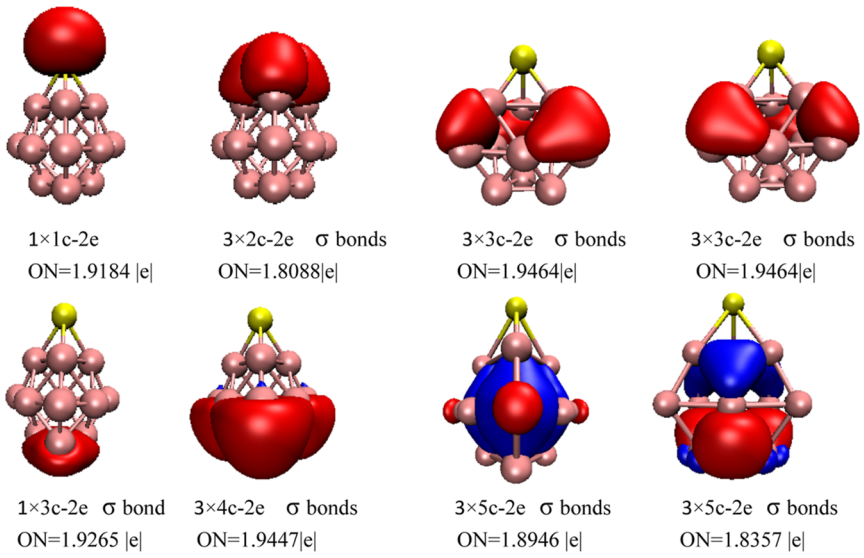

Figure 4. Bonding patterns of PB_{12}^{+}. The occupation numbers (ONs) are indicated and the yellow ball represents P atoms.

$P_2B_{12}^{+}$ adds an electron that occupies the β-LUMO of $P_2B_{12}^{+}$ and α-HOMO of $P_2B_{12}^{+}$, and β-LUMO of $P_2B_{12}^{+}$ combines into the HOMO of P_2B_{12}. Similar analyses can also be applied to PB_{12}^{-} and P_2B_{12}. The calculation results show that both HOMO and LUMO of P_2B_{12} are nondegenerate orbitals, this also prevents P_2B_{12} from lowering the symmetry due to the Jahn−Teller distortion after gaining or losing an electron; therefore, neutral, monocationic, and monoanionic $P_2B_{12}^{+/0/-}$ exhibit a D_{3h} symmetry.

With the adaptive natural density partitioning (AdNDP) method, we discussed the chemical bonding of closed-shell clusters in order to gain a deeper understanding of the stability of $P_nB_{12}^{+/0/-}$ (n = 1−2). For PB_{12}^{+} (Figure 4), there are one lone pair on the P atom, three 2c−2e σ bonds filling with the B−P bonds, six 3c−2e σ bonds distributed around six B_3 triangles around the side of the triangular bifrustum, one 3c−2e σ bond distributed around the B_3 triangle at the bottom of the triangular bifrustum, and three 4c−2e σ bonds distributed symmetrically around the side of the triangular bifrustum (the side without the P atom), three 5c−2e σ bonds distributed inside the triangular bifrustum, and three 5c−2e σ bonds distributed on the side surface of the triangular bifrustum in areas not filled by other bonds. Overall, three 2c−2e B−P bonds, seven 3c−2e B−B bonds, three 4c−2e σ bonds, and three 5c−2e σ bonds cover the edges and side surface of the PB_{12}^{+} construction, which renders stability to the PB_{12}^{+}, and three 5c−2e σ bonds distribute inside the molecule, which enhances the stability of PB_{12}^{+}. For P_2B_{12} (Figure 5), two lone pairs are on the P atoms and six 2c−2e σ bonds are on the B−P bonds. First, six 2c−2e σ bonds and six 4c−2e σ bonds fill with edges of a triangular bipyramid, which establishes stability to the P_2B_{12} cluster. Then, six 5c−2e σ bonds cover the entire side of triangular bifrustum, which renders stability to the P_2B_{12} cluster. Finally, three 5c−2e σ bonds distribute inside the triangular bifrustum, which enhances the stability of P_2B_{12}. Similar analysis can also be applied to PB_{12}^{-} (Figure 6). The P atom has five valence electrons, according to the above AdNDP bonding analyses of cage PB_{12}^{+} and P_2B_{12}, in addition to one lone pair, the other three electrons of the P atom combine with an electron of each B atom on the B_3 ring to form three 2c−2e σ bonds, and form three electron sharing

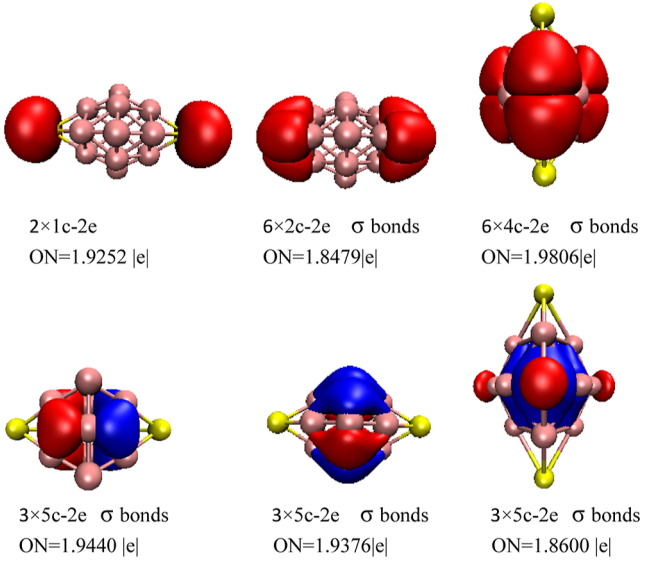

Figure 5. Bonding patterns of P_2B_{12}. The ONs are indicated and the yellow ball represents P atoms.

bonds with B atoms through covalent interactions, stabilizing the B_{12} cage. In addition, these delocalized π and σ bonds of $PB_{12}^{\pm}$ and P_2B_{12} indicate that the delocalized electron clouds distribute nearly equally throughout the molecule and effectively lessen the intramolecular electrostatic repulsion to some extent in the system, which is crucial to the stability. According to AdNDP investigations, the quasi-planar PB_{12}^{-} has 17 σ bonds and three π bonds, which surprisingly follow the $4m + 2$ Hückel rule for σ and π aromaticity. However, the cage PB_{12}^{+} and P_2B_{12} clusters possess 19 σ bonds and 21 σ bonds, respectively, which do not satisfy the spherical aromaticity [$2(n + 1)^2$ rule].

The spin density isosurface diagrams of open-shell clusters are displayed in Figure S11. The distribution of single electrons, or unpaired electrons, in the 3D space can be seen through spin density isosurface diagrams. α electrons are represented by green isosurface diagrams and β electrons by blue isosurface diagrams. For PB_{12}, the unpaired electrons are almost all α electrons, just a tiny percentage of the unpaired

https://doi.org/10.1021/acsomega.3c06002
ACS Omega 2023, 8, 44831−44838

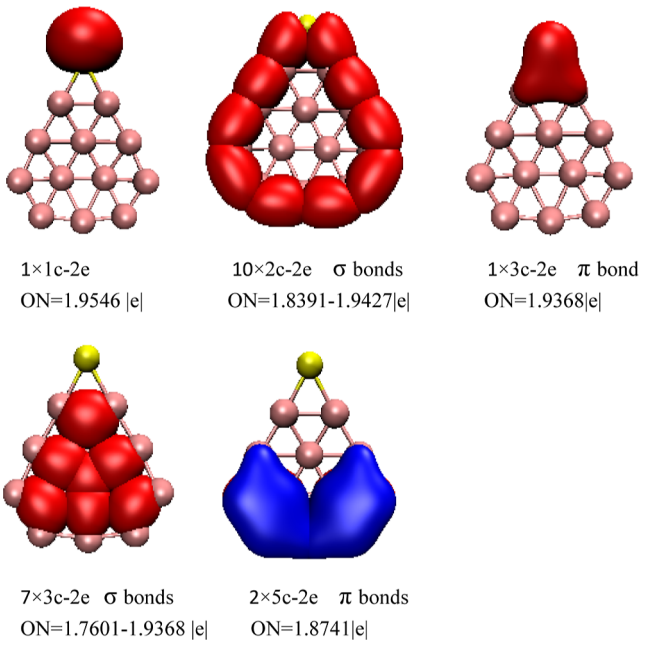

Figure 6. Bonding patterns of PB_{12}^-. The ONs are indicated and the yellow ball represents P atoms.

electrons are β electrons. Partial α electrons are distributed on the B atoms, and partial α electrons are distributed on the P atom. For $P_2B_{12}^+$, unpaired α electrons are distributed on the P atom and B atoms adjacent to phosphorus atoms; there are no unpaired β electrons. For $P_2B_{12}^-$, unpaired—electrons are distributed on the six B atoms in the middle of the triangular bipyramid. Furthermore, the spin density isosurface diagram of $P_2B_{12}^+$, α-HOMO of $P_2B_{12}^+$, and HOMO of P_2B_{12} have the same isosurface morphology because the HOMO orbital of P_2B_{12} becomes the single occupied α-HOMO of $P_2B_{12}^+$ after losing an electron from the HOMO orbital of P_2B_{12}. Similarly, the spin density isosurface diagram of $P_2B_{12}^-$, the α-HOMO of $P_2B_{12}^-$, and the LUMO of P_2B_{12} have the same isosurface morphology because P_2B_{12} adds an electron occupying the LUMO of P_2B_{12}, becoming the single-occupying α-HOMO of $P_2B_{12}^-$. It is anticipated that these spin characteristics will yield intriguing magnetic properties, which may also lead to molecular device applications. Furthermore, the spin density partially reflects the adsorption or chemical processes. The unpaired electrons of these clusters are mostly α electrons. B or P atoms with α single electrons can pair with free radicals or small molecules that have α single electrons, which is promising to form new covalent bonds.

3.2. Reactivity. The clusters show excellent properties in chemical reactions and chemical adsorption. Therefore, in chemical reactions or catalytic processes, predicting the active sites of electrophilic or nucleophilic reactions is significant in terms of theory and practicality aspects. The visualization of nucleophilic and electrophilic reactive sites can be predicted using the orbital-weighted dual descriptor.[50] Sites prone to nucleophilic reactions are represented by green isosurface maps in Figure 7, while sites prone to electrophilic reactions are represented by blue isosurface maps. Figure 7a shows that blue isosurface maps appear above the P atoms and B atoms adjacent to P atoms, which further reflects that two ends of the triangular bipyramid are most vulnerable to an electrophilic attack or, equivalently, the regions more nucleophilic. On the other hand, Figure 7a shows that green isosurface maps appear above the six B atoms in the middle of the triangular bipyramid, which further reflects that the six B atoms are most vulnerable to a nucleophilic attack, or equivalently, the regions are more electrophilic. Figure 7a also shows that the green isosurface maps of three B atoms are fatter than that of the other three B atoms, which indicates that the possibility of nucleophilic reaction is higher. PB_{12}^+ and P_2B_{12} have the same B_{12} cage, and Figure 7a,b also shows some of the same active site characteristics. However, due to the absence of a P atom in PB_{12}^+, PB_{12}^+, and P_2B_{12} have different active site characteristics, such as the three boron atoms in the middle of the triangular bipyramid changing from the nucleophilic reaction site to the electrophilic reaction site. Figure 7c shows that only blue isosurface maps appear above the P atom, which further reflects that the P atom is most vulnerable to an electrophilic attack. Although there are both green and blue isosurface maps distributed on the boron atoms of PB_{12}^-, they have obvious characteristics. Electrophilic reactions are more likely to occur when attacking from the molecular plane. Attacking from the direction perpendicular to the molecular plane, nucleophilic reactions are more likely to occur. Average local ionization energy (ALIE)[51,52] and local electron attachment energy (LEAE)[53] can be used to predict preferential reactive sites. As a comparison, we employ the ALIE and LEAE to analyze the cluster system above. The ALIE- and LEAE-mapped molecular van der Waals surface are shown in Figure S12. According to the comparative analysis (the detailed conclusion is shown in Figure S12), it can be seen that orbital-weighted dual descriptor analysis is reasonable and has the advantage of describing electrophilic and nucleophilic reaction sites simultaneously.

3.3. Photoelectron Spectra. Boron cluster geometrical configuration can be proved and identified by theoretical calculations combined with photoelectron spectroscopy.[4,9,54]

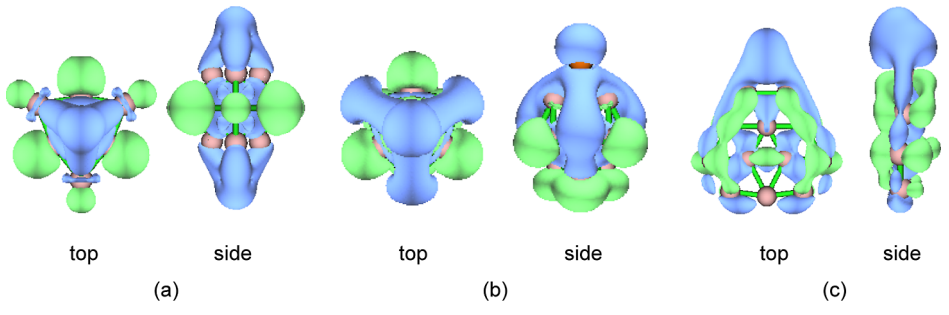

Figure 7. Orbital-weighted dual descriptor isograms; the isovalue is set to 0.001. (a) P_2B_{12}, (b) PB_{12}^+, and (c) PB_{12}^-.

https://doi.org/10.1021/acsomega.3c06002
ACS Omega 2023, 8, 44831−44838

Using the time-dependent DFT approach, we calculated the vertical detachment energies (VDEs) and simulated the photoelectron spectra of $P_nB_{12}^-$ (n = 1−2).[4,9,55] The photoelectron spectra of $P_nB_{12}^-$ (n = 1−2) are shown in Figure 8. According to the photoelectron spectra, $P_2B_{12}^-$ has

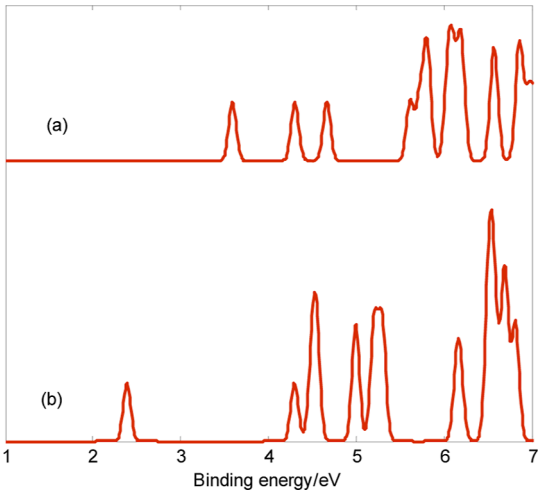

Figure 8. Calculated photoelectron spectra. (a) PB_{12}^-, and (b) $P_2B_{12}^-$.

the biggest energy gap (about 1.90 eV) between the first and second bands and the lowest first VDE. We will concentrate on the bands at the low binding energy side of photoelectron spectra because the first few bands were utilized to identify the geometrical configuration of boron clusters.[4,54] These photoelectron spectra's first peaks are derived from the calculated ground-state VDEs of PB_{12}^- and $P_2B_{12}^-$ at 3.59 and 2.39 eV, respectively. The calculated ground-state VDE of closed-shell PB_{12}^- originates from the detachment of the electron from the molecular orbital (HOMO). For open-shell $P_2B_{12}^-$, the calculated ground-state VDE of $P_2B_{12}^-$ derives from the electrons being detached from the molecular orbital α-HOMO. The second calculated VDE at 4.30 eV, which results from separating the electrons from HOMO − 1, is the source of the second peak of PB_{12}^-. The third calculated VDE at 4.67 eV, which results from separating the electrons from HOMO − 2, is where the third peak of PB_{12}^- originates. The second peak of $P_2B_{12}^-$ comes from the second VDE at 4.29 eV, which originates from the electrons being detached from β-HOMO. Furthermore, the peaks with larger binding energy derive from the electrons being detached from lower molecular orbitals. $P_nB_{12}^-$ (n = 1−2) contain distinct spectral features, as shown in Figure 8, particularly distinct spectral bands at the low binding energy side. Important information for the identification of $P_nB_{12}^-$ (n = 1−2) is provided by these features.

4. CONCLUSIONS

The conclusions of the study are mainly summarized in the following aspects. (1) One and two P atoms doping can cause the B_{12} motif to the smallest B_{12} cage, composed of two B_3 rings at both ends and one B_6 ring in the middle, forming a triangular bifrustum, and the P atom is attached to the B_3 ring. (2) The neutral, monocationic, and monoanionic clusters $P_2B_{12}^{+/0/-}$ exhibit a high symmetry of D_{3h}, showing the same cage structure at the same time reported until now. (3) According to AdNDP bonding analyses of cage PB_{12}^+ and P_2B_{12}, one P atom can combine with three B atoms to form three electron sharing bonds through covalent interactions, stabilizing the B_{12} cage. (4) The electronic and geometric properties of these clusters are promising to provide a theoretical basis for applications in the chemical reaction and single-molecule device. (5) Photoelectron spectra of $P_nB_{12}^-$ (n = 1−2) have different spectral bands at the low binding energy side that can be compared with future experimental values. This research enriches a new database of geometrical structures of doped boron clusters.

■ ASSOCIATED CONTENT

Supporting Information

The Supporting Information is available free of charge at https://pubs.acs.org/doi/10.1021/acsomega.3c06002.

Different isomers of $P_nB_{12}^{+/0/-}$ (n = 1−2), relative energies (eV) of cage structure and quasi-planar structure PB_{12}^+, geometrical parameters of $P_2B_{12}^{+/0/-}$, rmsd versus time of PB_{12}^+, P_2B_{12}, $P_2B_{12}^+$, and $P_2B_{12}^-$, selected CMOs of $P_2B_{12}^{+/0/-}$, spin density of PB_{12}, $P_2B_{12}^+$, and $P_2B_{12}^-$, and ALIE and LEAE mapped van der Waals surface (PDF)

■ AUTHOR INFORMATION

Corresponding Author

Shi-Xiong Li − *School of Physics and Electronic Science, Guizhou Education University, Guiyang 550018, China;* orcid.org/0000-0003-2831-5955; Email: leesxoptics@163.com

Authors

Yue-Ju Yang − *School of Physics and Electronic Science, Guizhou Education University, Guiyang 550018, China*

De-Liang Chen − *School of Physics and Electronic Science, Guizhou Education University, Guiyang 550018, China*

Complete contact information is available at: https://pubs.acs.org/10.1021/acsomega.3c06002

Notes

The authors declare no competing financial interest.

■ ACKNOWLEDGMENTS

This work was supported by the Central Guiding Local Science and Technology Development Foundation of China (grant no. QK ZYD[2019]4012), and the Growth Foundation for Young Scientists of Education Department of Guizhou Province (grant no. QJH KY[2022]310, QJJ [2022]260), China.

■ REFERENCES

(1) Sergeeva, A. P.; Popov, I. A.; Piazza, Z. A.; Li, W. L.; Romanescu, C.; Wang, L. S.; Boldyrev, A. I. Understanding boron through size-selected clusters: structure, chemical bonding, and fluxionality. *Acc. Chem. Res.* **2014**, *47*, 1349−1358.

(2) Jian, T.; Chen, X.; Li, S. D.; Boldyrev, A. I.; Li, J.; Wang, L. S. Probing the structures and bonding of size-selected boron and doped-boron clusters. *Chem. Soc. Rev.* **2019**, *48*, 3550−3591.

(3) Alexandrova, A. N.; Boldyrev, A. I.; Zhai, H.-J.; Wang, L.-S. All-boron aromatic clusters as potential new inorganic ligands and building blocks in chemistry. *Coord. Chem. Rev.* **2006**, *250*, 2811−2866.

(4) Zhai, H. J.; Zhao, Y. F.; Li, W. L.; Chen, Q.; Bai, H.; Hu, H. S.; Piazza, Z. A.; Tian, W. J.; Lu, H. G.; Wu, Y. B.; Mu, Y. W.; Wei, G. F.;

https://doi.org/10.1021/acsomega.3c06002
ACS Omega 2023, 8, 44831−44838

Liu, Z. P.; Li, J.; Li, S. D.; Wang, L. S. Observation of an all-boron fullerene. *Nat. Chem.* **2014**, *6*, 727−731.
(5) Tai, T. B.; Duong, L. V.; Pham, H. T.; Mai, D. T.; Nguyen, M. T. A disk-aromatic bowl cluster B_{30}: toward formation of boron buckyballs. *Chem. Commun.* **2014**, *50*, 1558−1560.
(6) Tai, T. B.; Nguyen, M. T. The B_{32} cluster has the most stable bowl structure with a remarkable heptagonal hole. *Chem. Commun.* **2015**, *51*, 7677−7680.
(7) Tai, T. B.; Nguyen, M. T. A new chiral boron cluster B_{44} containing nonagonal holes. *Chem. Commun.* **2016**, *52*, 1653−1656.
(8) Chen, T. T.; Li, W. L.; Chen, W. J.; Li, J.; Wang, L. S. $La_3B_{14}^-$: an inverse triple-decker lanthanide boron cluster. *Chem. Commun.* **2019**, *55*, 7864−7867.
(9) Chen, Q.; Li, W. L.; Zhao, Y. F.; Zhang, S. Y.; Hu, H. S.; Bai, H.; Li, H. R.; Tian, W. J.; Lu, H. G.; Zhai, H. J.; Li, S. D.; Li, J.; Wang, L. S. Experimental and theoretical evidence of an axially chiral borospherene. *ACS Nano* **2015**, *9*, 754−760.
(10) Mannix, A. J.; Zhou, X. F.; Kiraly, B.; Wood, J. D.; Alducin, D.; Myers, B. D.; Liu, X.; Fisher, B. L.; Santiago, U.; Guest, J. R.; Yacaman, M. J.; Ponce, A.; Oganov, A. R.; Hersam, M. C.; Guisinger, N. P. Synthesis of borophenes: Anisotropic, two-dimensional boron polymorphs. *Science* **2015**, *350*, 1513−1516.
(11) Li, Q.; Kolluru, V. S. C.; Rahn, M. S.; Schwenker, E.; Li, S.; Hennig, R. G.; Darancet, P.; Chan, M. K. Y.; Hersam, M. C. Synthesis of borophane polymorphs through hydrogenation of borophene. *Science* **2021**, *371*, 1143−1148.
(12) Li, W. L.; Jian, T.; Chen, X.; Li, H. R.; Chen, T. T.; Luo, X. M.; Li, S. D.; Li, J.; Wang, L. S. Observation of a metal-centered B_2^- Ta@B_{18}^- tubular molecular rotor and a perfect Ta@B_{20}^- boron drum with the record coordination number of twenty. *Chem. Commun.* **2017**, *53*, 1587−1590.
(13) Chen, W. J.; Zhang, Y. Y.; Li, W. L.; Choi, H. W.; Li, J.; Wang, L. S. AuB_8^-: an Au-borozene complex. *Chem. Commun.* **2022**, *58*, 3134−3137.
(14) Barroso, J.; Pan, S.; Merino, G. Structural transformations in boron clusters induced by metal doping. *Chem. Soc. Rev.* **2022**, *51*, 1098−1123.
(15) Đorđević, S.; Radenković, S. Electronic structure, stability, and aromaticity of M_2B_6 (M = Mg, Ca, Sr, and Ba): an interplay between spin pairing and electron delocalization. *Phys. Chem. Chem. Phys.* **2022**, *24*, 5833−5841.
(16) Li, S. X.; Yang, Y. J.; Chen, D. L.; Long, Z. W. Structures, and electronic and spectral properties of single-atom transition metal-doped boron clusters MB_{24}^-(M = Sc, Ti, V, Cr, Mn, Fe, Co, and Ni). *RSC Adv.* **2022**, *12*, 16706−16716.
(17) Lv, J.; Wang, Y.; Zhang, L.; Lin, H.; Zhao, J.; Ma, Y. Stabilization of fullerene-like boron cages by transition metal encapsulation. *Nanoscale* **2015**, *7*, 10482−10489.
(18) Wei, D.; Ren, M.; Lu, C.; Bi, J.; Maroulis, G. A quasi-plane IrB_{18}^- cluster with high stability. *Phys. Chem. Chem. Phys.* **2020**, *22*, 5942−5948.
(19) Tian, Y.; Wei, D.; Jin, Y.; Barroso, J.; Lu, C.; Merino, G. Exhaustive exploration of MgBn (n = 10−20) clusters and their anions. *Phys. Chem. Chem. Phys.* **2019**, *21*, 6935−6941.
(20) Tam, N. M.; Duong, L. V.; Pham, H. T.; Nguyen, M. T.; Pham-Ho, M. P. Effects of single and double nickel doping on boron clusters: stabilization of tubular structures in BnNim, n = 2−22, m = 1, 2. *Phys. Chem. Chem. Phys.* **2019**, *21*, 8365−8375.
(21) Ren, M.; Jin, S.; Wei, D.; Jin, Y.; Tian, Y.; Lu, C.; Gutsev, G. L. NbB_{12}^-: a new member of half-sandwich type doped boron clusters with high stability. *Phys. Chem. Chem. Phys.* **2019**, *21*, 21746−21752.
(22) Chen, T. T.; Li, W. L.; Chen, W. J.; Yu, X. H.; Dong, X. R.; Li, J.; Wang, L. S. Spherical trihedral metallo-borospherenes. *Nat. Commun.* **2020**, *11*, 2766.
(23) Yan, L. Large B_7 Triangles in Hollow Spherical Trihedral Metallo-borospherenes and Their Endohedral Complexes of $B_{20}TM_n$(TM = Sc, Y; n = 3, 4): a Theoretical Characterization. *Inorg. Chem.* **2022**, *61*, 10652−10660.
(24) Zhang, Y.; Lu, X. Q.; Yan, M.; Li, S. D. Perfect Spherical Tetrahedral Metallo-Borospherene Ta_4B_{18} as a Superatom Following the 18-Electron Rule. *ACS Omega* **2021**, *6*, 10991−10996.
(25) Dong, X.; Jalife, S.; Vasquez-Espinal, A.; Ravell, E.; Pan, S.; Cabellos, J. L.; Liang, W. Y.; Cui, Z. H.; Merino, G. Li_2B_{12} and Li_3B_{12}: Prediction of the Smallest Tubular and Cage-like Boron Structures. *Angew. Chem., Int. Ed.* **2018**, *57*, 4627−4631.
(26) Zhang, Y.; Zhao, X. Y.; Yan, M.; Li, S. D. From inverse sandwich $Ta_2B_7^+$ and Ta_2B_8 to spherical trihedral $Ta_3B_{12}^-$: prediction of the smallest metallo-borospherene. *RSC Adv.* **2020**, *10*, 29320−29325.
(27) Dong, X.; Liu, Y. Q.; Liu, X. B.; Pan, S.; Cui, Z. H.; Merino, G. Be_4 B_{12}^+: A Covalently Bonded Archimedean Beryllo-Borospherene. *Angew. Chem., Int. Ed.* **2022**, *61*, No. e202208152.
(28) Bai, H.; Bai, B.; Zhang, L.; Huang, W.; Zhai, H. J.; Li, S. D. $B_{12}F_n^{0/-}$ (n = 1−6) series: when do boron double chain nanoribbons become global minima? *Phys. Chem. Chem. Phys.* **2017**, *19*, 31655−31665.
(29) Van Duong, L.; Tho Nguyen, M. Silicon doped boron clusters: how to make stable ribbons? *Phys. Chem. Chem. Phys.* **2017**, *19*, 14913−14918.
(30) Li, P. F.; Zhai, H. J. Structures and chemical bonding of boron-based $B_{12}O$ and $B_{11}Au$ clusters. A counterexample in boronyl chemistry. *Phys. Chem. Chem. Phys.* **2022**, *24*, 10952−10961.
(31) Yang, Y. J.; Li, S. X.; Chen, D. L.; Long, Z. W. Structural Evolution and Electronic Properties of Selenium-Doped Boron Clusters $SeB_n^{0/-}$ (n = 3−16). *Molecules* **2023**, *28*, 357.
(32) Sun, R.; Jin, B.; Huo, B.; Yuan, C.; Zhai, H. J.; Wu, Y. B. Planar pentacoordinate carbon in a sulphur-surrounded boron wheel: the global minimum of CB_5S_5. *Chem. Commun.* **2022**, *58*, 2552−2555.
(33) Cui, Z. H.; Contreras, M.; Ding, Y. H.; Merino, G. Planar tetracoordinate carbon versus planar tetracoordinate boron: the case of CB4 and its cation. *J. Am. Chem. Soc.* **2011**, *133*, 13228−13231.
(34) Lv, J.; Wang, Y.; Zhu, L.; Ma, Y. Particle-swarm structure prediction on clusters. *J. Chem. Phys.* **2012**, *137*, 084104.
(35) Lv, J.; Wang, Y.; Zhu, L.; Ma, Y. B38: an all-boron fullerene analogue. *Nanoscale* **2014**, *6*, 11692−11696.
(36) Liang, W. Y.; Das, A.; Dong, X.; Cui, Z. H. Lithium doped tubular structure in LiB_{20} and LiB_{20}^-: a viable global minimum. *Phys. Chem. Chem. Phys.* **2018**, *20*, 16202−16208.
(37) Adamo, C.; Barone, V. Toward reliable density functional methods without adjustable parameters: The PBE0 model. *J. Chem. Phys.* **1999**, *110*, 6158−6170.
(38) Krishnan, R.; Binkley, J. S.; Seeger, R.; Pople, J. A. Self-consistent molecular orbital methods. XX. A basis set for correlated wave functions. *J. Chem. Phys.* **1980**, *72*, 650−654.
(39) Weigend, F.; Ahlrichs, R. Balanced basis sets of split valence, triple zeta valence and quadruple zeta valence quality for H to Rn: Design and assessment of accuracy. *Phys. Chem. Chem. Phys.* **2005**, *7*, 3297−3305.
(40) Tao, J.; Perdew, J. P.; Staroverov, V. N.; Scuseria, G. E. Climbing the density functional ladder: nonempirical meta-generalized gradient approximation designed for molecules and solids. *Phys. Rev. Lett.* **2003**, *91*, 146401.
(41) Bartlett, R. J.; Musiał, M. Coupled-cluster theory in quantum chemistry. *Rev. Mod. Phys.* **2007**, *79*, 291−352.
(42) Chen, B. L.; Sun, W. G.; Kuang, X. Y.; Lu, C.; Xia, X. X.; Shi, H. X.; Maroulis, G. Structural Stability and Evolution of Medium-Sized Tantalum-Doped Boron Clusters: A Half-Sandwich-Structured TaB_{12}^- Cluster. *Inorg. Chem.* **2018**, *57*, 343−350.
(43) Li, P.; Du, X.; Wang, J. J.; Lu, C.; Chen, H. Probing the Structural Evolution and Stabilities of Medium-Sized $MoB_n^{0/-}$ Clusters. *J. Phys. Chem. C* **2018**, *122*, 20000−20005.
(44) Jin, S.; Chen, B.; Kuang, X.; Lu, C.; Sun, W.; Xia, X.; Gutsev, G. L. Structural and Electronic Properties of Medium-Sized Aluminum-Doped Boron Clusters AlB_n and Their Anions. *J. Phys. Chem. C* **2019**, *123*, 6276−6283.
(45) Frisch, M. J.; Trucks, G. W.; Schlegel, H. B.; Scuseria, G. E.; Robb, M. A.; Cheeseman, J. R.; Scalmani, G.; Barone, V.; Petersson,

https://doi.org/10.1021/acsomega.3c06002
ACS Omega 2023, 8, 44831−44838

G. A.; Nakatsuji, H.; et al. *Gaussian 16*; Gaussian Inc.: Wallingford, CT, USA, 2016.
(46) Lu, T.; Chen, F. Multiwfn: A multifunctional wavefunction analyzer. *J. Comput. Chem.* **2012**, *33*, 580−592.
(47) Humphrey, W.; Dalke, A.; Schulten, K. VMD: Visual molecular dynamics. *J. Mol. Graph.* **1996**, *14*, 33−38.
(48) Schlegel, H. B.; Millam, J. M.; Iyengar, S. S.; Voth, G. A.; Daniels, A. D.; Scuseria, G. E.; Frisch, M. J. Ab initio molecular dynamics: Propagating the density matrix with Gaussian orbitals. *J. Chem. Phys.* **2001**, *114*, 9758−9763.
(49) Schlegel, H. B.; Iyengar, S. S.; Li, X.; Millam, J. M.; Voth, G. A.; Scuseria, G. E.; Frisch, M. J. Ab initio molecular dynamics: Propagating the density matrix with Gaussian orbitals. III. Comparison with Born−Oppenheimer dynamics. *J. Chem. Phys.* **2002**, *117*, 8694−8704.
(50) Pino-Rios, R.; Inostroza, D.; Cardenas-Jiron, G.; Tiznado, W. Orbital-Weighted Dual Descriptor for the Study of Local Reactivity of Systems with (Quasi-) Degenerate States. *J. Phys. Chem. A* **2019**, *123*, 10556−10562.
(51) Sjoberg, P.; Murray, J. S.; Brinck, T.; Politzer, P. Average local ionization energies on the molecular surfaces of aromatic systems as guides to chemical reactivity. *Can. J. Chem.* **1990**, *68*, 1440−1443.
(52) Politzer, P.; Murray, J. S.; Bulat, F. A. Average local ionization energy: A review. *J. Mol. Model.* **2010**, *16*, 1731−1742.
(53) Brinck, T.; Carlqvist, P.; Stenlid, J. H. Local Electron Attachment Energy and Its Use for Predicting Nucleophilic Reactions and Halogen Bonding. *J. Phys. Chem. A* **2016**, *120*, 10023−10032.
(54) Zhai, H. J.; Kiran, B.; Li, J.; Wang, L. S. Hydrocarbon analogues of boron clusters−planarity, aromaticity and antiaromaticity. *Nat. Mater.* **2003**, *2*, 827−833.
(55) Bauernschmitt, R.; Ahlrichs, R. Treatment of electronic excitations within the adiabatic approximation of time dependent density functional theory. *Chem. Phys. Lett.* **1996**, *256*, 454−464.

https://doi.org/10.1021/acsomega.3c06002
ACS Omega 2023, 8, 44831−44838